Enigmatic very-low-frequency tremors beneath the Shonai Plain in northeastern Japan

K. Nishida[1] and K. Shiomi[2]

K. Nishida, Earthquake Research Institute, University of Tokyo, 1-1-1 Yayoi 1, Bunkyo-ku, Tokyo 113-0032, Japan (knishida@eri.u-tokyo.ac.jp)

K. Shiomi, National Research Institute for Earth Science and Disaster Prevention, Tsukuba 305-0006, Japan

[1]Earthquake Research Institute, University of Tokyo, Tokyo, Japan

[2]National Research Institute for Earth Science and Disaster Prevention, Tsukuba, Japan

Abstract. Recently, dense and sensitive modern seismic networks have revealed tectonic and volcanic tremors. Although most studies of seismic tremors focused on these two types, other types of tremor activities also exist. For detecting such tremor activities, we analyzed data from the Hi-net high-sensitivity accelerometers (tiltmeters) between June 2004 and June 2006. The results elucidate very-low-frequency (VLF) Love-wave tremors with a typical frequency of 0.085 Hz beneath the Shonai Plain in northeastern Japan. The tremor activity lasted for several days and occurred several times per month in winter. The activity was triggered by secondary microseisms, which provide a proxy for local ocean swell activity. A possible source is a sub-horizontal crack coupled with a fluid reservoir at the bottom of the sedimentary layer. All the observed features suggest that hydrologic phenomena are potential sources of VLF tremors. Because similar hydrologic phenomena can be expected even in tectonically and volcanically inactive regions, modern array observations by broadband seismometers may reveal similar hydrologic tremors in such regions.

1. Introduction

Over the past decade, a new generation of dense and sensitive seismic networks has developed. These networks led to the discovery of non-volcanic tremors in 2002 [*Obara*, 2002]. They also revealed related phenomena over a wide frequency range: low-frequency earthquakes [*Katsumata and Kamaya*, 2003] (1–10 Hz) and very-low-frequency (VLF) earthquakes [*Ito et al.*, 2007] (0.01–0.1 Hz). Now, these phenomena are recognized as members of a family of slow earthquakes related to shear slip in subduction zones [*Beroza and Ide*, 2011].

Volcanic fluid systems also excite seismic tremors. Recent observations by broadband seismometers show a wide variety of monotonic waveforms for tremors or those having several spectral peaks over a wide frequency range lasting for minutes, hours, or sometimes even days. These observations are clues for understanding the physical conditions and dynamic states of volcanic edifices and volcanic fluid systems [*McNutt*, 2005; *Kawakatsu and Yamamoto*, 2007].

Although most studies on seismic tremors have focused on these two types, other types of VLF tremor activities also exist. One example involves enigmatic VLF tremors in the Gulf of Guinea [*Oliver*, 1962; *Shapiro et al.*, 2006]. Persistent Rayleigh waves with a period of 26 s were observed at broadband stations in the US, Europe, and Africa during the Southern Hemispheric winter. The physical cause of these waves remains unclear, partly because of sparse station distribution near the source. We searched for such enigmatic tremor activities in northeastern Japan using a modern dense seismic network.

2. Observation of VLF Love-wave tremors

For the detection of non-tectonic and non-volcanic VLF tremors (0.01–0.1 Hz), we analyzed data from the Hi-net tiltmeters [*Okada et al.*, 2004] operated by the National Research Institute for Earth Science and Disaster Prevention. The tiltmeters can be used as a dense network of horizontal long-period seismometers [*Tonegawa et al.*, 2006].

We discovered enigmatic VLF tremor activities beneath the Shonai Plain in northeastern Japan (Fig. 1). In this region, the Pacific plate subducts westward beneath the North American plate. The Shonai Plain is at the northern end of the Niigata–Kobe Tectonic Zone [*Sagiya et al.*, 2000], which is a zone of high-strain rates as revealed by a GPS array in Japan. The Shonai Plain is underlain by thick Middle Miocene mafic submarine volcanic rocks covered by younger sediments with a thickness of about 2 km [*Sato and Amano*, 1991], and it is also an estuarine region of the Mogami River. Magnetotelluric data revealed a shallow conductive sedimentary layer (1–10 ohm·m) beneath the Shonai Plain. The layer connects to an eastward-dipping, elongates conductor along the Shonai Plain fault zone [*Ichihara et al.*, 2011], and probably represents the existence of fluid there.

Fig. 2 shows a typical example of tremor records for December 6, 2004; the records were bandpass filtered from 0.05 to 0.1 Hz. The tremor activity lasted for three days. The transverse and radial components of the tremors were plotted against their distance from an assumed tremor source shown in Fig. 1. The plot of transverse components shows persistent wave propagation up to 200 km, whereas that of radial components does not show any propagation (Fig. 2(b)). Surprisingly, the plots suggest dominance of Love-wave tremors in transverse components. The plot of transverse components from 0.1 to 0.5 Hz

(Fig. 2(c)) does not show any propagation, due to dominance of background surface waves known as micorseisms [*Longuet-Higgins*, 1950].

Fig. 1 also shows a plot of polarization ellipses of horizontal motions at stations, which were computed by solving eigen problems for covariance matrices between the horizontal components [*Jurkevics*, 1988]. The sizes of the ellipses represent the mean squared amplitudes with correction of geometrical spreading of surface waves. Ellipticities for most ellipses are high, and directions of the major axes are perpendicular to the directions of propagation. These results also show the dominance in transverse components. In addition, we can identify a two-lobed radiation pattern, although the azimuthal coverage is incomplete.

To estimate precise phase velocities and amplitudes of the observed waves, we calculated wavenumber–frequency spectra with an assumed source as follows. The surface wave acceleration wave field for a point source can be represented by

$$a_\theta(\Theta, \Phi, \omega) = \frac{1}{\sqrt{\sin\Theta}} V_R(\Phi, \omega) e^{-i\omega\Theta/c_R(\omega)}, \quad (1)$$

$$a_\phi(\Theta, \Phi, \omega) = \frac{1}{\sqrt{\sin\Theta}} V_L(\Phi, \omega) e^{-i\omega\Theta/c_L(\omega)}, \quad (2)$$

where a_θ is a radial component of acceleration, a_ϕ is a transverse component, Θ is the epicentral distance, Φ is the azimuth as shown in Fig. 3, c is an assumed phase velocity, ω is the angular frequency, V represents radiation properties at the source, R denotes Rayleigh waves, and L denotes Love waves. At a station with an epicentral distance shorter than 150 km, the observed record was back-propagated to the source with an assumed phase velocity. We assume that back-propagated records at ith station (V_R and

V_L)were modeled by a two-lobed radiation pattern as

$$V_R(\Phi_i, \omega) = v_R^0(\omega)\cos(\Phi_i) + v_R^1(\omega)\sin(\Phi_i), \tag{3}$$

$$V_L(\Phi_i, \omega) = v_L^0(\omega)\cos(\Phi_i) + v_L^1(\omega)\sin(\Phi_i). \tag{4}$$

We estimated V_R and V_L by minimizing the residual sum of squares between the observed records and the model at every frequency and phase velocity.

Fig. 4 shows the plots of ensemble averages $\langle |v_R^0|^2 + |v_R^1|^2 \rangle$ and $\langle |v_L^0|^2 + |v_L^1|^2 \rangle$ on December 6 2004 against the assumed frequencies and phase velocities, producing wavenumber–frequency spectra. Fig. 4(a) shows the spectrum of radial components and Fig. 4(b) shows that of transverse components. Fig. 4(a) shows Rayleigh wave propagation with a phase velocity of about 3 km/s, whereas Fig. 4(b) shows Love-wave propagation with a phase velocity of about 3.5 km/s. The dominant frequency of these waves is about 0.09 Hz. The power spectrum density of the Love waves at the peak is an order of magnitude larger than that of the Rayleigh waves. The dominance of the Love wave is not easily explained by reference to the usual seismic sources, including landslides and volcanic eruptions.

3. Effects of a sedimentary layer on excitations of Love and Rayleigh waves

The key to understand the dominance of the Love waves is an insight into the sedimentary layer. The phase velocity of a crustal Rayleigh wave in the frequency range 0.05-0.1 Hz ($\sim$3.2 km/s) is closer to the P-wave velocity of the sedimentary layer ($\sim$2.2 km/s) than to the S-wave velocity ($\sim$1.0 km/s) in this area [*Koketsu et al.*, 2008]. Therefore, the crustal Rayleigh wave is coupled with a sedimentary P-wave, whereas the crustal Love wave is coupled with a sedimentary S-wave. In this case, a source in the sedimentary layer excites the crustal Love wave more efficiently than the crustal Rayleigh wave.

Here, we consider the Love-wave excitation quantitatively. We assume a point source represented by a moment tensor at the origin of polar coordinates (Fig. 3). Surface wave acceleration fields in laterally and slowly varying media can be written in terms of surface wave potentials [*Dahlen and Tromp*, 1998]. For simplicity, we assume a local 1-D model, except around the source. The 1-D model was constructed from a 3-D crustal model based on ambient noise tomography [*Nishida et al.*, 2008a]. Around the source, we introduced a 2-km-thick sedimentary layer [*Koketsu et al.*, 2008] into the model, as shown in Fig. 5. The acceleration wave field can be described by Eq. 1. In this case, V_R and V_L can be given as follows:

$$
\begin{aligned}
V_R(\Phi,\omega) &= S_R M_{rr} + P_R \frac{M_{\theta\theta}+M_{\phi\phi}}{2} + iQ_R(M_{r\theta}\cos\Phi + M_{r\phi}\sin\Phi) \\
&+ P_R\left(\frac{M_{\theta\theta}-M_{\phi\phi}}{2}\cos 2\Phi + M_{\theta\phi}\sin 2\Phi\right) \qquad (5)\\
V_L(\Phi,\omega) &= iQ_L(-M_{r\phi}\cos\Phi + M_{r\theta}\sin\Phi) \\
&- P_L\left(M_{\theta\phi}\cos 2\Phi - \frac{M_{\theta\theta}-M_{\phi\phi}}{2}\sin 2\Phi\right), \qquad (6)
\end{aligned}
$$

where M_{ij} is the ijth component of the moment tensor. Here, P_R, Q_R, S_R, Q_L, and P_L are moment tensor response functions [*Dahlen and Tromp*, 1998]. The moment response functions can be represented by source and propagation terms using local eigen functions at the source and receivers, respectively. Fig. 5 shows these functions at 0.085 Hz and the S-wave and P-wave velocity models in this study. Because Q_L is much larger than the other functions at a depth of 2 km, the enhancement of Love-wave excitation by a deeper source becomes more significant. This result means that the source should be near the bottom of the sedimentary layer.

To understand the dominance of Love-wave excitation, we show an asymptotic representation of the moment response. Here, we assume a horizontal shear fault (or the conjugate vertical fault) for simplicity, because a corresponding component Q_L is dominant. A shallow, horizontal shear fault with seismic moment M_0 at depth z can be approximated by a horizontal point force on the surface [*Dahlen*, 1993], with a Love-wave force F_L and a Rayleigh wave force F_R given as follows:

$$F_L = \frac{\omega^2 M_0 z}{\beta^2 c_L^2}(c_L^2 - \beta^2) \quad (7)$$

$$F_R = \frac{\omega^2 M_0 z}{\beta^2 c_R^2}\left(c_R^2 - \frac{1-2\nu}{(1-\nu)^2}\alpha^2\right), \quad (8)$$

where α is P-wave velocity, β is the shear-wave velocity, and ν is the Poisson ratio within the sedimentary layer. Eq. (8) shows that Rayleigh wave excitation is negligible when the P-wave velocity in the sedimentary layer matches the phase velocity of the Rayleigh wave. Here, we assume that the Poisson ratio of many earth materials (ν) can be approximated to 1/4. Within the sedimentary layer, this wave behaves like a P-wave propagating in the horizontal direction. We note that this wave is similar to a shear-coupled leaky P (PL) wave [*Oliver*, 1961].

In the shallowest part of the sedimentary layer, the radiation of Love waves from a subhorizontal shear fault is sensitive to small changes in the dip angle of the fault [*Fukao*, 1979; *Fukao*, 1995], because P_L is much larger than Q_L near the surface. However, a horizontal shear fault near the bottom of the sedimentary layer is less sensitive to the dip angle, because Q_L is much larger than P_L at that depth, as shown in Fig. 5. Because of the insensitivity at depth, we cannot determine other components of the moment tensor.

4. Source locations of the VLF tremors

To locate the centroids of the tremors, we selected 26 stations within a 100-km radius of the assumed source (Fig. 1). For each station, we removed glitches and divided all the records from June 2004 to June 2006 into 1024 s segments with an overlap of 512 s. To analyze the background wavefield, we discarded transient phenomena such as earthquakes and local noise. We assume a double-couple source at the bottom of the sedimentary layer as shown in Fig. 3. One force couple is vertical and the other is horizontal because the double-couple component has greater sensitivity than the other components as shown in the previous section.

We inferred source locations, source time functions, and azimuths of horizontal force couples by maximizing the variance reduction (VR) between synthetics and observed data, which is a method similar to the GridMT technique [*Kawakatsu*, 1998]. Here, we used only transverse components from 0.05 to 0.1 Hz because of the small amplitudes of the Rayleigh waves. With the assumption of the double-couple source at the basement of the sedimentary layer (2 km), the transverse component of the synthetic acceleration wavefield a_ϕ can be simplified by a two-lobed radiation pattern as follows:

$$a_\phi(\Theta, \Phi) = \frac{f(\omega)}{\sqrt{\sin\Theta}} i Q_L(\omega) \sin(\Phi - \lambda) e^{i\omega\Theta/c_L(\omega)}, \tag{9}$$

where λ is the azimuth of a horizontal force couple and $f(\omega)$ is the Fourier transform of a moment rate function.

To calculate VR, we conducted an iterative inversion. One iteration incorporates the following two steps. First, we chose an initial value of azimuth λ. For λ, we estimate the moment rate function f as

$$f(\omega) = \frac{\sum_j d_j a_\phi^*(\Theta_j, \Phi_j) \sin\Theta_j}{\sum_j a_\phi(\Theta_j, \Phi_j) a_\phi^*(\Theta_j, \Phi_j) \sin\Theta_j}, \tag{10}$$

where d_j represents the observed transverse components at the jth station. Next, for the estimated moment rate function f, the azimuth of the horizontal force couple is calculated by solving the following equation:

$$\begin{pmatrix} \cos\Phi_0 & \sin\Phi_0 \\ \cos\Phi_1 & \sin\Phi_1 \\ \vdots & \vdots \\ \cos\Phi_n & \sin\Phi_n \end{pmatrix} \begin{pmatrix} \sin\lambda \\ \cos\lambda \end{pmatrix} = \Im \begin{pmatrix} \sqrt{\sin\Theta_0} \frac{\sum_i f^*(\omega_i) d_0(\omega_i) e^{-i\omega_i \Theta_0 / C_L(\omega_i)}}{\sum_i f(\omega_i) f^*(\omega_i)} \\ \sqrt{\sin\Theta_1} \frac{\sum_i f^*(\omega_i) d_1(\omega_i) e^{-i\omega_i \Theta_1 / C_L(\omega_i)}}{\sum_i f(\omega_i) f^*(\omega_i)} \\ \vdots \\ \sqrt{\sin\Theta_n} \frac{\sum_i f^*(\omega_i) d_n(\omega_i) e^{-i\omega_i \Theta_n / C_L(\omega_i)}}{\sum_i f(\omega_i) f^*(\omega_i)} \end{pmatrix}, \tag{11}$$

where $-\pi/2 < \lambda < \pi/2$, and $\Im()$ represents the imaginary part. After 10 iterations of these two steps, we calculated VR of the data. Then, we estimated the locations of the tremor at the global maximum of VR.

To verify the assumption that the two-lobed pattern is dominant, we plotted the imaginary part of the right hand terms of Eq. (11), as shown in Fig. 6. Here, we used typical records of December 6, 2004. This figure shows a clear two-lobed pattern although the azimuthal coverage is incomplete.

We conducted a two-step grid search for the global maximum of VRs. First, we searched for the maximum at coarse grid spacing with horizontal spatial intervals of 5×10^{-2} degrees (Fig. 8). Next, around the coarse grid, we searched for the maximum at fine grid spacing with intervals of 1×10^{-3} degrees. The centroid of the source was located at the grid point with the maximum VR. To estimate the location error, we made 50 bootstrap samples and estimated the error ellipse of 1σ. The detection criteria for the tremor included a maximum VR greater than 85% and a mean bootstrap epicenter error smaller than 2 km. Fig. 7 shows typical source locations with error ellipses. The ellipses are elongated perpendicular to the coastline because the stations are distributed only on the land side.

Fig. 8 shows centroid locations of the detected tremors. The tremors were located at a point in shallow water at depth of about 30 m near the shoreline, which is an estuarine region of the Mogami River. Bathymetry slopes in this region are gentle. The tremors did not migrate temporally within the accuracy of about 2 km.

In Fig. 9, the mean power spectrum for source time functions of the detected tremors shows a clear peak with dominant frequency of about 0.085 Hz. The observed dominant frequency did not fluctuate with time. Above 0.11 Hz, we did not detect any tremor signal, although we cannot rule out a possibility that large background noise masks tiny tremor signals. The observed monochromatic peak implies an excitation mechanism associated with the resonance of a fluid system such as volcanic tremors [*Kawakatsu and Yamamoto*, 2007].

Fig. 10(a) shows the moment rates of the tremors plotted against time. Here, we define the moment rates by root-mean-square amplitudes (RMSs) of the source time functions. Many tremors occurred in winter, and few events occurred in summer. The moment rates were of the order of 10^{11} [Nm/s]. Each cluster of the detected events represents one period of tremor activity. An enlarged plot of December 2004 shows three clusters of tremor activity with a typical duration of about 1–2 days (Fig. 10(b)). They occurred several times per month, only in winter. We did not identify any correlation between the activity and tide as in low-frequency tremors [*Nakata et al.*, 2008]. We also plotted azimuths of the horizontal force couples against time, as shown in Fig. 10(a). These azimuths were around 120° and did not change for the entire period.

5. Triggering by microseisms

Here, we consider the possibility that the tremor activity was trigged by microseisms. Microseisms are background Love and Rayleigh waves excited by ocean swell activity. They exhibit two distinct peaks at the primary and secondary frequencies: the primary microseisms at around 0.1 Hz have been interpreted as being caused by direct loading of ocean swell onto a sloping beach [*Haubrich et al.*, 1963]; the typical frequency of the secondary microseisms at about 0.2 Hz approximately doubles the typical frequency of ocean swells, indicating the generation of the former through non-linear wave–wave interaction of the latter [*Longuet-Higgins*, 1950]. Because the amplitudes of secondary microseisms are much larger than those of primary microseisms, they provide a proxy for local ocean swell activity. We overlaid RMSs of the secondary microseisms from 0.2 to 0.4 Hz in Fig. 10(b). The detected tremors occurred in periods of high microseism activity.

To verify the relationship between the two activities over the entire period, we plotted estimated moment rates of the tremors against RMS of the secondary microseisms in Fig. 11. Here, we note that we plotted not only detected events (red points) but also quiet periods with less tremor activity (black points); these did not satisfy the detection criteria of the tremors. A cluster of detected events is well separated from quiet periods with little tremor activity (black points). Actual moment rates of the tremors in quiet periods should be smaller than the estimated ones, because the estimated ones are apparent owing to primary microseisms. This figure shows that the detected tremors occurred in periods of high ocean swell activity throughout the period. This relationship suggests that ocean swells triggered tremor activity throughout the period.

6. Discussion on the excitation mechanisms of the tremors

On the basis of these observed features, we will discuss four possible excitation mechanisms for the tremors: (1) primary microseisms, (2) volcanic tremors, (3) tectonic origin, and (4) hydrologic tremors.

6.1. Primary microseisms

In this area, primary microseisms originate from the Pacific Ocean and the Japan Sea. Their typical frequencies strongly depend on local ocean swell activity. In most cases, the typical frequency of the microseisms from the Japan Sea is higher than that from the Pacific Ocean, because ocean swell in a closed sea (the Japan Sea) is fetch-limited compared to that in the open ocean (the Pacific Ocean). Observed frequencies of significant ocean waves at Sakata (Fig. 1) fluctuated with time in contrast to the detected tremors, and were always higher than 0.1 Hz in December 2004 (Nationwide Ocean Wave information network for Ports and Harbours [*Nagai et al.*, 1994]). Peak frequencies of the primary microseisms from the Japan Sea were higher than those of the tremors.

Tidal resonance of the swell at a topographic anomaly is another candidate. However, the tidal changes in this area are small because the Japan sea is a semi-closed sea surrounded by the continent of Asia and the islands of Japan [*Odamaki*, 1989], and the topographic changes in the region are gentle. If tidal resonance was a valid mechanism, the excitation sources could be represented by shear traction at the anomaly [*Fukao et al.*, 2010; *Saito*, 2010]. In this case, the ratio of mean-squared amplitudes of Raleigh waves to those of Love wave is estimated to be 0.2 with the eigen functions used in this study.

For comparison with observations, we estimate the ratios for all detected tremors. For estimation of Rayleigh wave amplitudes, we applied the inversion method for not only transverse components but also radial components with fixed source locations. We used stations within a 150-km radius of the source locations to detect smaller Rayleigh wave signals. Fig. 12 illustrates that ratios were about 0.05 throughout the period. The estimated ratios are significantly smaller than the theoretical prediction of the shear traction of 0.2. The ratios of the tremors are also significantly smaller than those of primary microseisms in Japan, which were estimated to be about 0.5 [*Nishida et al.*, 2008b]. On the other hand, the double-couple source model in this study can explain the observed ratios shown in Fig. 12. Thus, we can rule out the possibility that primary microseisms excited the tremors directly.

6.2. Volcanic tremors

The nearest active volcano, Mt. Chokai, is 30 km away from the source location of the detected tremors. Moreover, no volcanic earthquakes or tremors have been reported since the last eruption of Mt. Chokai in 1974. Therefore, we can rule out the possibility of volcanic tremors.

6.3. Tectonic origin

Next, we consider the possibility of a tectonic origin. The study area is at the northern end of the Niigata–Kobe Tectonic Zone [*Sagiya et al.*, 2000], which is a zone of high-strain rates revealed by a GPS array in Japan. The contraction rate is several times larger than that of the surrounding regions. We discuss the possibility that the excitation source is periodic stick-slip owing to this contraction.

With a simple assumption of periodic stick-slip faulting with recurrence frequency, f_0 of 0.085 Hz, the moment release rate $M(t)$ at time t can be modeled as

$$M(t) = M_0 \sin(2\pi f_0 t) + M_1 t, \qquad (12)$$

where M_0 is the mean moment rate of detected tremors and M_1 is an unobserved long-term component. Because $M(t)$ should be positive, M_1 should be at least larger than M_0. Moment release over the entire period (two years) can be estimated by the cumulative moment release of M_1. The estimated lower limit of the moment release is 4×10^{17} [Nm]. Assuming that the fault size is 10 km $\times$ 10 km at its maximum and the shear modulus in the sedimentary layer is 2 $\times10^9$ [Pa], the slip rate should be larger than 1 m/year. This value is beyond the contraction rate. Even if the slip rate were true, the resultant surface displacement should be observed by GPS in the region. Because the corresponding surface displacements have not been observed, we can rule out this possibility.

6.4. Hydrologic tremors

We consider a hydrologic excitation mechanism using a sub-horizontal crack model along an aquifer coupled with a fluid reservoir, as shown in Fig. 8. When the movement of fluid from the reservoir to the crack excites seismic waves, the source can be represented by a sub-vertical compensated linear vector dipole (CLVD) [*Knopoff and Randall*, 1970].

We consider excitation by the sub-vertical CLVD source quantitatively. With the assumption of a small dip angle, η, of the sub-horizontal crack, moment response functions V_R and V_L can be written as

$$\begin{aligned} V_R(\Phi,\omega) &= M_0\left(\left(-\frac{2S_R}{3}+\frac{P_R}{3}\right)+iQ_R\eta\sin(\Phi+\lambda)\right) \\ V_L(\Phi,\omega) &= -M_0 iQ_L\eta\cos(\Phi+\lambda), \end{aligned} \qquad (13)$$

where η is the dip angle of the crack and M_0 is the moment release rate of the sub-vertical CLVD. Fig. 13 shows the geometry of the sub–horizontal crack. Because $(-\frac{2S_R}{3} + \frac{P_R}{3})$ in the equation is negligible at depth (Fig. 14), the excitation of the surface waves by the CLVD source is represented by the modeled double–couple source. We note that we can constrain only ηM_0 in this model. The estimated azimuth of the horizontal force couple represents the dip direction of the crack λ in this model. The source locations were at the western boundary of the thick sedimentary area [*Koketsu et al.*, 2008] (Fig. 8). This fact suggests that the western inclined edge of an aquifer is a possible source of the tremors. This model can also explain the absence of temporal variations of the locations and azimuths (Fig. 10(a)).

On the basis of the hydrologic excitation mechanism, we discuss trigger mechanisms. There are two possibilities: one is that fluid flowed from the surface to the crack as a result of ocean swells, and the other is that elastic stress change was caused by secondary microseisms. The former can be ruled out because pressure fluctuations cannot reach the source region instantaneously at depths of the order of 1 km. In this case, we consider the latter mechanism. The secondary microseisms are mainly composed of background Rayleigh waves [*Nishida et al.*, 2008b], which cause dilation in the sedimentary layer. We can estimate periodic elastic stress changes due to secondary microseisms by the eigen function of Rayleigh waves at the relevant frequency. They are of the order of 10 Pa at the source depth. The periodic stress changes of about 0.2 Hz lasted for several days. Because the dilatation opens apertures of fluid paths in the sedimentary layer, extruded fluid is supplied to the source region [*Brodsky and Prejean*, 2005; *Miyazawa and Brodsky*, 2008]. When the cumulative supplies reach a certain level of fluid volume, the tremor may be triggered. Note that we did not confirm dynamic triggering by large earthquakes (e.g., the Sumatra–Andaman earthquake in 2004), as shown in Fig. 10(b). Elastic stress changes due to large earthquakes (Mw > 8) are of the order of 10 kPa [*Miyazawa and Brodsky*, 2008]; however, the transient stress change with larger wavelength may not be enough to trigger the tremor.

Similar but much stronger VLF tremors were observed at broadband stations in the US, Europe, and Africa [*Oliver*, 1962; *Shapiro et al.*, 2006]. They originated in the equatorial Atlantic near the African coast (the Gulf of Guinea). Although Rayleigh wave excitation was dominant in this case, they exhibit three similar features: (1) a narrow spectral peak at 0.038 Hz, (2) clear seasonal variations with maximum amplitudes in the Southern Hemisphere winter, and (3) thick sediments (3000–6000 m) at the source region [*Laske and Masters*, 1997]. Although their physical cause remains unclear, this study suggests that a similar hydrologic phenomenon is a possible source. Similar hydrologic phenomena can be expected in the absence of tectonic or volcanic activities. Modern array observations by broadband seismometers may reveal similar hydrologic tremors even in tectonically and volcanically inactive regions.

7. Conclusions

We found unreported VLF Love-wave tremors beneath the Shonai Plain in northeastern Japan. The dominance of Love waves suggests that their excitation source should be located at the basement of the sedimentary layer. We analyzed records of the Hi-net tiltmeter data from June 2004 to June 2006 at 26 stations within a 100-km radius of the assumed source. We inferred source locations by maximizing VR between the observed data and synthetics with an assumption of a double-couple source. The detected tremors were located at a point in an estuarine region of the Mogami River with an accuracy of about 2 km. Tremor activity with a duration of several days occurred several times per month only in winter. Tremors did not migrate temporally within the accuracy. The azimuths of the modeled force couples did not change from around 120° throughout the period. Estimated source time functions show a clear monochromatic peak at 0.085 Hz. The typical moment rates of the tremors were of the order of 10^{11} [Nm/s]. Tremor activity was triggered by secondary microseisms, which provide a proxy for local ocean swell activity. On the basis of these observed features, we discussed four possible excitation mechanisms for the tremors: (1) direct excitation by primary microseisms, (2) volcanic tremors, (3) tectonic origin, and (4) a hydrologic origin. We can rule out the first possibility because typical frequencies of microseisms were lower than those of tremors. We can also rule out the second possibility because active volcanoes are very far from the source locations. The third mechanism (tectonic origin) is improbable because an expected slip rate is beyond the contraction rate in this region. The fourth mechanism of a hydrologic origin is possible. A sub-horizontal crack coupled with a fluid reservoir at the bottom of the sedimentary layer can explain all the observed features. This result suggests that hydrologic phenomena are potential sources of VLF tremors even in tectonically and volcanically inactive areas.

Acknowledgments. This study is supported by KAKENHI (22740289). The authors thank H. Kawakatsu and N. Shapiro for the constructive discussions that contributed to this study. We also thank two anonymous reviewers for many constructive comments. Maps were generated using the generic mapping tools (GMT) software package [*Wessel and Smith*, 1998].

References

Beroza, G. C., and S. Ide (2011), Slow Earthquakes and Nonvolcanic Tremor, *Annu. Rev. Earth Planet. Sci.*, *39*, 271–296, doi:10.1146/annurev-earth-040809-152531.

Brodsky, E. E., and S. G. Prejean (2005), New constraints on mechanisms of remotely triggered seismicity at Long Valley Caldera, *J. Geophys. Res.*, *110*(B9), B04302, doi: 10.1029/2004JB003211.

Dahlen, F. (1993), Single-force representation of shallow landslide sources, *Bull. Seismol. Soc. Am.*, *83*(1), 130–143.

Dahlen, F., and J. Tromp (1998), *Theoretical Global Seismology*, 1025, Princeton University Press, Princeton.

Fukao, Y. (1979), Tsunami earthquakes and subduction processes near deep-sea trenches, *J. Geophys. Res.*, *84*, 2303–2314, doi:10.1029/JB084iB05p02303.

Fukao, Y. (1995), Single-force representation of earthquakes due to landslides or the collapse of caverns, *Geophys. J. Int.*, *122*(1), 243–248, doi:10.1111/j.1365-246X.1995.tb03551.x.

Fukao, Y., K. Nishida, N. Kobayashi (2010), Seafloor topography, ocean infragravity waves and background Love and Rayleigh waves, *J. Geohpys. Res.*, *115*, B04302, doi: 10.1029/2009JB006678.

Haubrich, R., W. Munk, and F. Snodgrass (1963), Comparative spectra of microseisms and swell, *Bull. Seismol. Soc. Am.*, *53*, 27–37.

Ichihara, H., et al. (2011), A fault-zone conductor beneath a compressional inversion zone, northeastern Honshu, Japan, *Geophys. Res. Lett.*, *38*(9), 38–41, doi: 10.1029/2011GL047382.

Ito, Y., K. Obara, K. Shiomi, S. Sekine, and H. Hirose (2007), Slow Earthquakes Coincident with Episodic Tremors and Slow Slip Events, *Science*, *315*, 503–506, doi: 10.1126/science.1134454.

Jurkevics, A. (1988), Polarization analysis of three-component array data, *Bull. Seismol. Soc. Am.*, *78*(5), 1725–1743.

Katsumata, A., and N. Kamaya (2003), Low-frequency continuous tremor around the Moho discontinuity away from volcanoes in the southwest Japan, *Geophys. Res. Lett.*, *30*(1), 1020, doi:10.1029/2002GL015981.

Kawakatsu, H. (1998), On the realtime monitoring of the long-period seismic wavefield, *Bull. Earthquake Res. Inst.*, *73*, 267–268.

Kawakatsu, H., and M. Yamamoto (2007), Volcano Seismology, in *Treatise on Geophysics: Earthquake Seismology*, edited by G. Schubert, 389–420, Oxford: Elsevier, doi:10.1016/B978-044452748-6.00073-0.

Knopoff, L., and M. J. Randall (1970), The Compensated Linear-Vector Dipole: A Possible Mechanism for Deep Earthquakes, *J. Geophys. Res.*, *75*, 4957–4963, doi: 10.1029/JB075i026p04957.

Koketsu, K., H. Miyake, H. Fujiwara, and T. Hashimoto (2008), Progress towards a Japan integrated velocity structure model and long-period ground motion hazard map, in *Proceedings of the 14th World Conf. Earthq. Eng*, 1–7.

Laske, G., and G. Masters (1997), A global digital map of sediment thickness, *Eos Trans. AGU*, (78), F483.

Longuet-Higgins, M. (1950), A theory of the origin of microseisms, *Phil. Trans. of the Roy. Soc. of London*, *243*, 1–35.

McNutt, S. R. (2005), Volcanic Seismology, *Annu. Rev. Earth Planet. Sci.*, *33*(1), 461–491, doi:10.1146/annurev.earth.33.092203.122459.

Miyazawa, M., and E. E. Brodsky (2008), Deep low-frequency tremor that correlates with passing surface waves, *J. Geophys. Res.*, *113*(B12), B01307, doi:10.1029/2006JB004890.

Nagai, T., K. Sugahara, N. Hashimoto, T. Asai, S. Higashiyama, and K. Toda (1994), Introduction of Japanese NOWPHAS system and its recent topics, in *Proceedings of the International Conference on Hydro-Technical Engineering for Port and Harbor Construction (HYDRO-PORT'94), PHRI*, 67–82.

Nakata, R., N. Suda, and H. Tsuruoka (2008), Non-volcanic tremor resulting from the combined effect of Earth tides and slow slip events, *Nature Geoscience*, *1*(10), 676–678, doi:10.1038/ngeo288.

Nishida, K., H. Kawakatsu, and K. Obara (2008), Three-dimensional crustal S wave velocity structure in Japan using microseismic data recorded by Hi-net tiltmeters, *J. Geophys. Res.*, *113*(B12), B10302, doi:10.1029/2007JB005395.

Nishida, K., H. Kawakatsu, Y. Fukao, and K. Obara (2008), Background Love and Rayleigh waves simultaneously generated at the Pacific Ocean floors, *Geophys. Res. Lett.*, *35*(16), L16307.

Obara, K. (2002), Nonvolcanic Deep Tremor Associated with Subduction in Southwest Japan, *Science*, *296*, 1679–1681, doi:10.1126/science.1070378.

Odamaki, M. (1989), Co-Oscillating and Independent Tides of the Japan Sea, *J. Oceanographical Soc. Japan*, *45*, 217–232.

Okada, Y., K. Kasahara, S. Hori, K. Obara, S. Sekiguchi, H. Fujiwara, and A. Yamamoto (2004), Recent progress of seismic observation networks in Japan: Hi-net, F-net, K-NET and KiK-net, *Earth, Planets, and Space*, *56*, D15.

Oliver, J. (1961), On the long period character of shear waves, *Bull. Seismol. Soc. Am.*, *51*(1), 1–12.

Oliver, J. (1962), A world wide storm of microseisms with periods of about 27 second seconds, *Bull. Seismol. Soc. Am.*, *52*(3), 507–517.

Sagiya, T., S. Miyazaki, and T. Tada (2000), Continuous GPS Array and Present-day Crustal Deformation of Japan, *Pure Appl. Geophys.*, *157*, 2303–2322.

Saito, T. (2010), Love wave excitation due to the interaction between a propagating ocean wave and the sea-bottom topography, *Geophys. J. Int.*, *182*, doi:10.1111/j.1365-246X.2010.04695.

Sato, H., and K. Amano (1991), Relationship between tectonics, volcanism, sedimentation and basin development, Late Cenozoic, central part of Northern Honshu, Japan, *Sedimentary Geology*, *74*(1-4), 323–343, doi:10.1016/0037-0738(91)90071-K.

Shapiro, N. M., M. H. Ritzwoller, and G. D. Bensen (2006), Source location of the 26 sec microseism from cross-correlations of ambient seismic noise, *Geophys. Res. Lett.*, *331*, L18310, doi:10.1029/2006GL027010.

Tonegawa, T., K. Hirahara, and K. Shiomi (2006), Upper mantle imaging beneath the Japan Islands by Hi-net tiltmeter recordings, *Eath Planet Space*, *58*, 1007–1012.

Wessel, P., and W. Smith (1998), New, improved version of Generic Mapping Tools released, *EOS transactions*, *79*, 579–579.

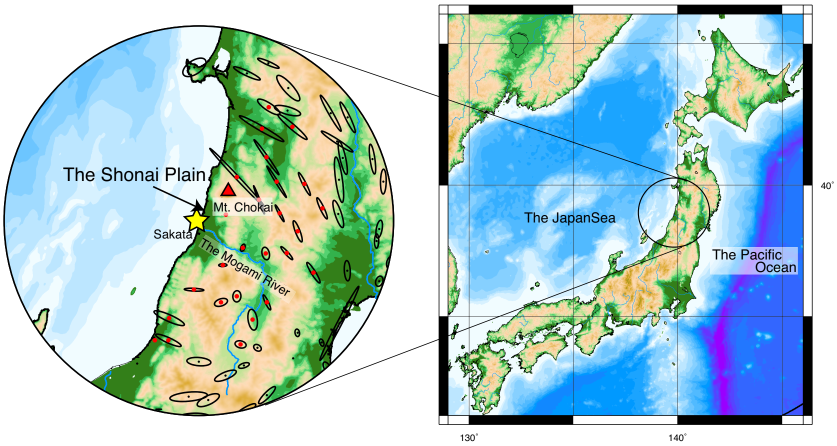

Figure 1. Location map of 26 Hi-net stations used in this study (red points). We also show a typical example of particle motions at Hi-net stations on December 6, 2004. The yellow star symbol represents an assumed source.

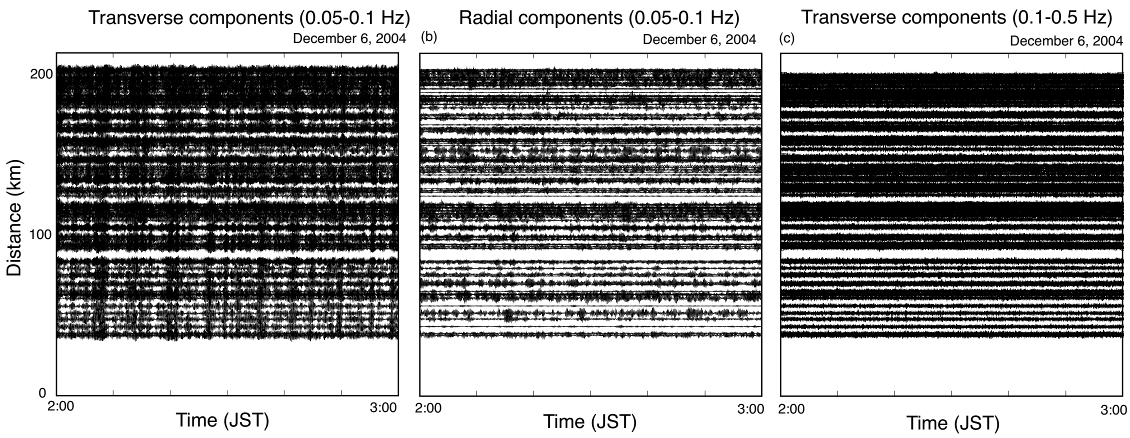

Figure 2. (a) Recorded section of transverse components (perpendicular to the propagation direction) bandpass filtered from 0.05 to 0.1 Hz on December 6, 2004 with a typical source location shown by a star symbol in Fig. 1. The vertical axis shows their distance from the assumed source. (b) Record section of radial components (parallel to the propagation direction) in the same frequency range. (c) Record section of transverse components bandpass filtered from 0.1 to 0.5 Hz corresponding to secondary microseisms [*Longuet-Higgins*, 1950].

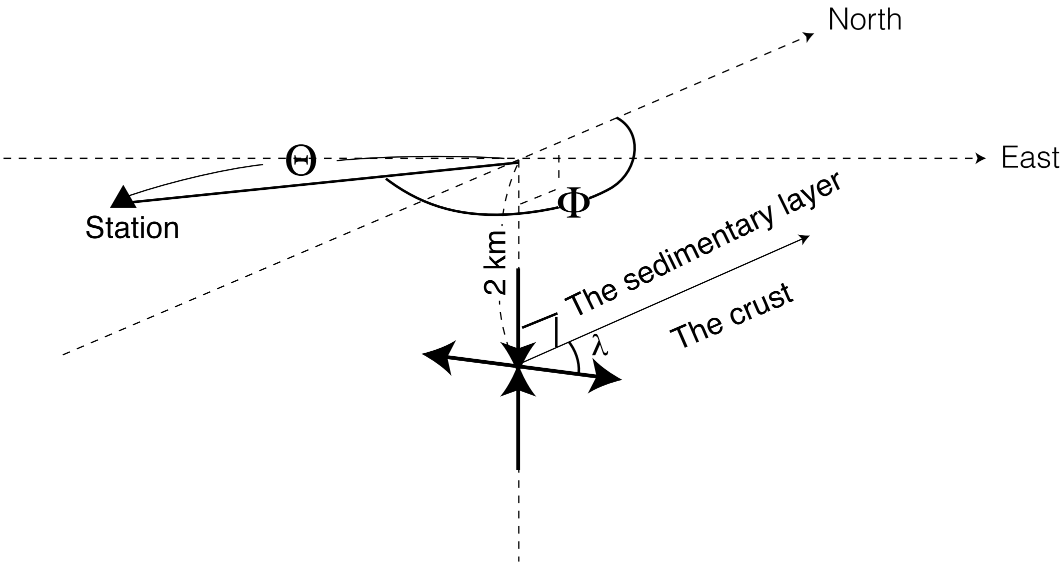

Figure 3. Schematic of the coordinates used in this study.

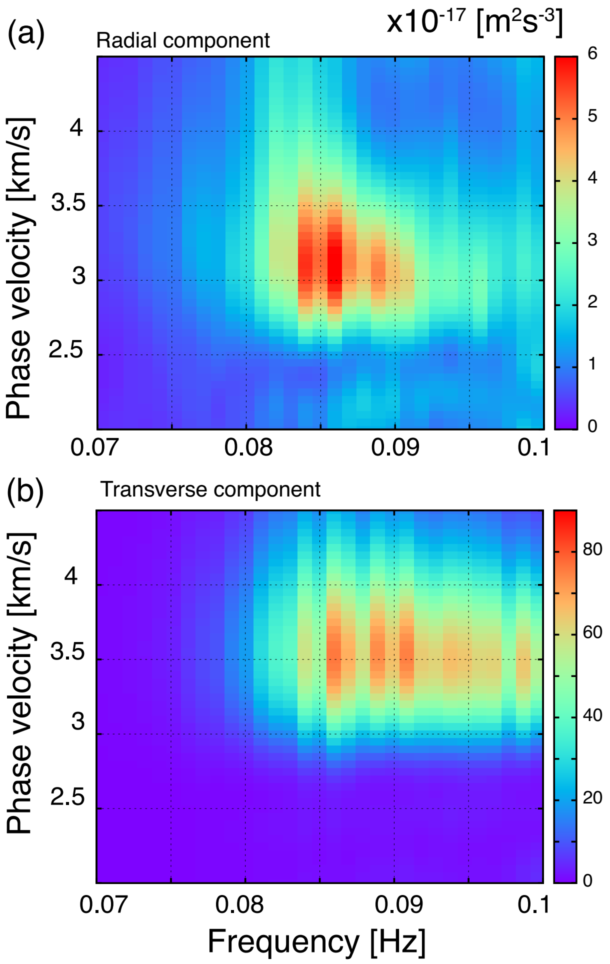

Figure 4. (a) Wavenumber–frequency spectrum of radial components on December 6, 2004 with a typical source location. Vertical axis shows phase velocity and horizontal axis shows frequency. The spectrum shows Rayleigh wave propagation. (b) Wavenumber–frequency spectrum of transverse components. This spectrum shows Love-wave propagation. Power spectral densities of Love waves are an order of magnitude larger than those of Rayleigh waves.

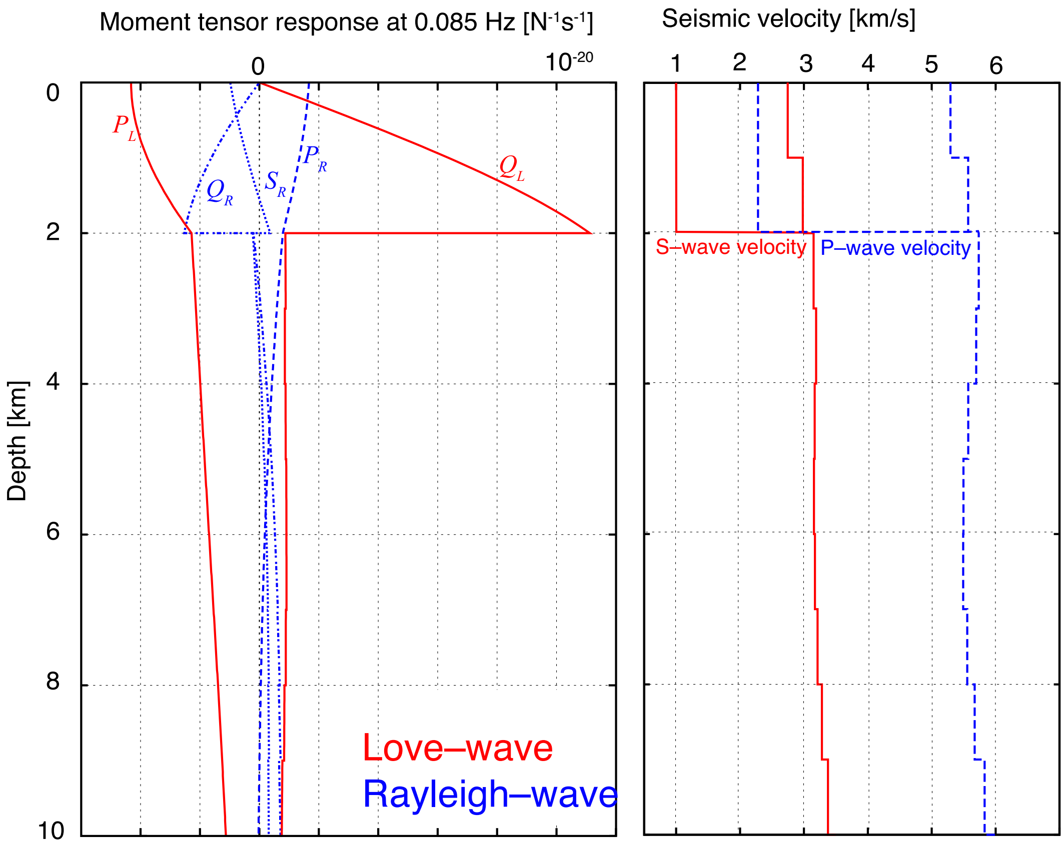

Figure 5. (a) Moment tensor response functions. (b) P-wave and S-wave velocity models with and without the sedimentary layer used in this study.

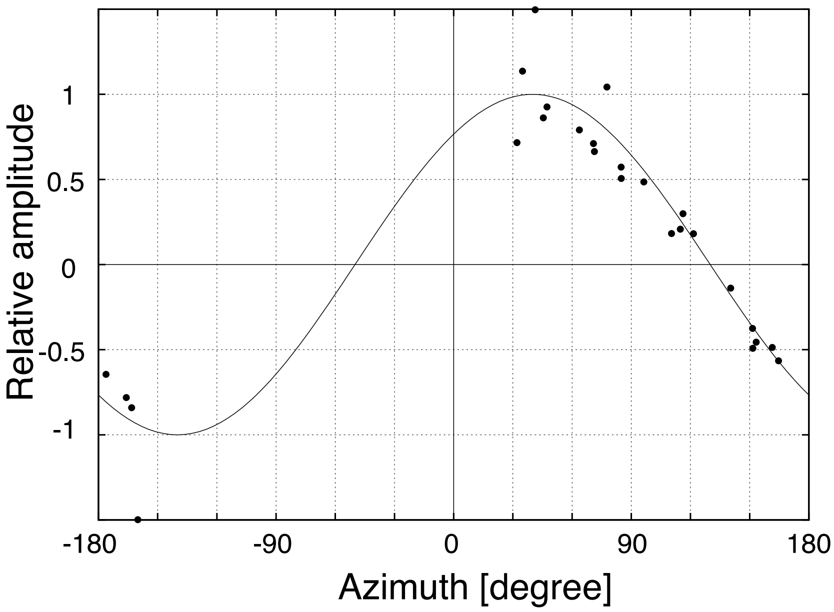

Figure 6. Relative amplitudes at stations as shown in Eq. (11) plotted against their azimuths. Here, we show a typical result for December 6, 2004. We also plotted the best-fit curve, which shows that the observed data can be explained by a two-lobed pattern.

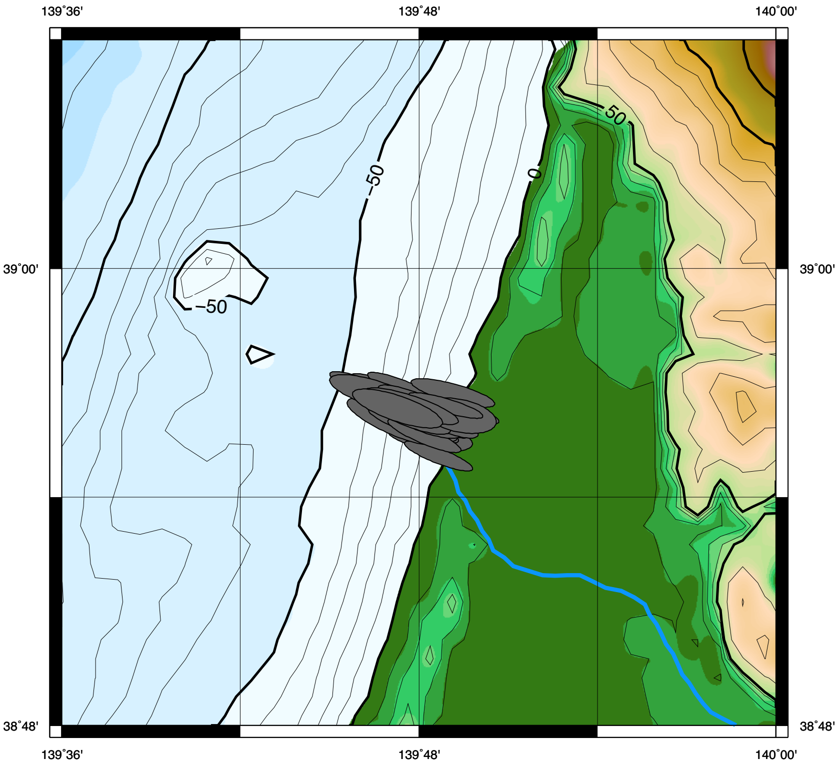

Figure 7. Typical source locations of detected events with error ellipses of 1σ. The ellipses are elongated perpendicular to the coastline because of incomplete station distribution and were located in the shore region at depths shallower than 50 m.

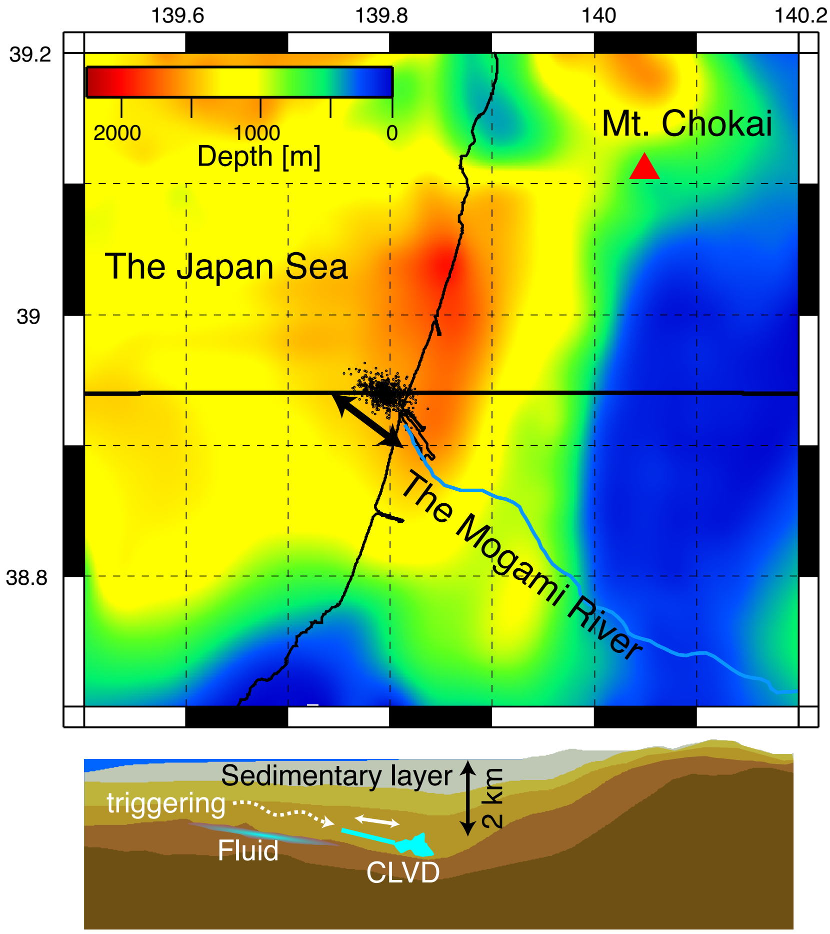

Figure 8. Detected events and depth distribution of the top of the sedimentary layer with S-wave velocity of 2 km/s [*Koketsu et al.*, 2008]. The events were located beneath the Shonai Plain in northeastern Japan. We plotted a typical azimuth of the horizontal force couple. We also show a schematic of a depth section along the thick line shown in the figure. Beneath the Shonai Plain, a 2-km-thick sediment layer was assumed [*Koketsu et al.*, 2008]. In this area, the water depth is so shallow that we can neglect the effects of the water column.

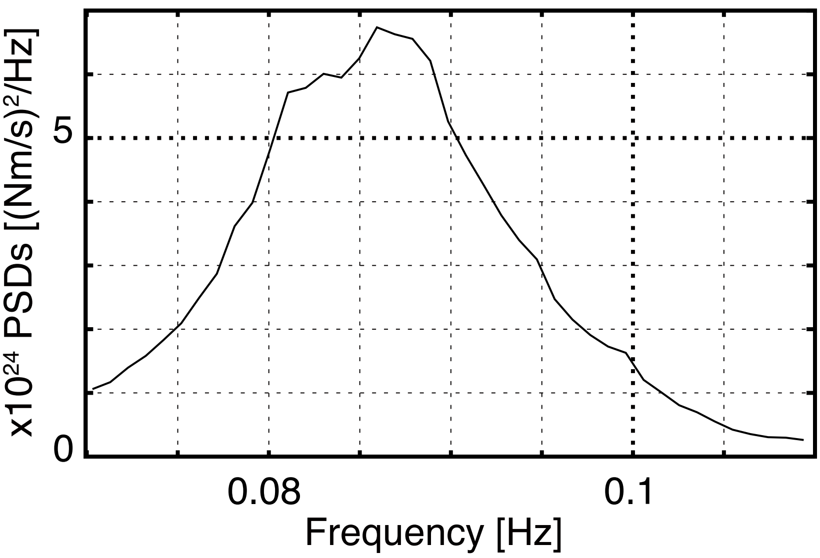

Figure 9. Mean power spectrum of moment rate functions. The spectrum shows the monotonic excitation with a typical frequency of about 0.085 Hz.

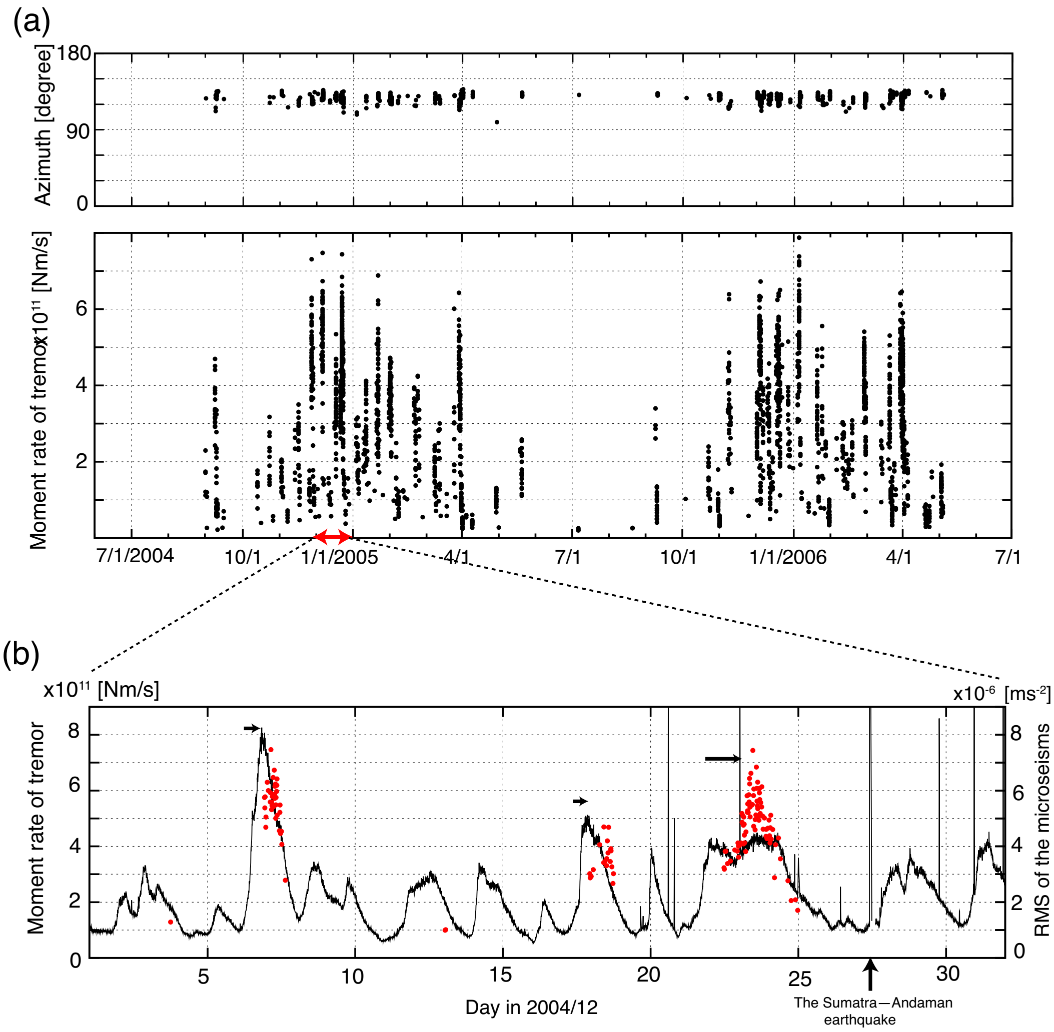

Figure 10. (a) Plot of RMSs of moment release rates of detected events against time. We also plotted azimuths of horizontal force couples of detected events against time. (b) Enlarged plot of (a) for December 2004. Red dots represent the detected events. We also plotted RMSs from 0.2 to 0.4 Hz, which are a proxy for oceanic swell activity in this area. The background ground motions are known as secondary microseisms. Clusters of the detected events started at a peak of ocean swell activity. We note that tremor activity was not triggered by the 2004 Sumatra–Andaman earthquake (Mw 9.2).

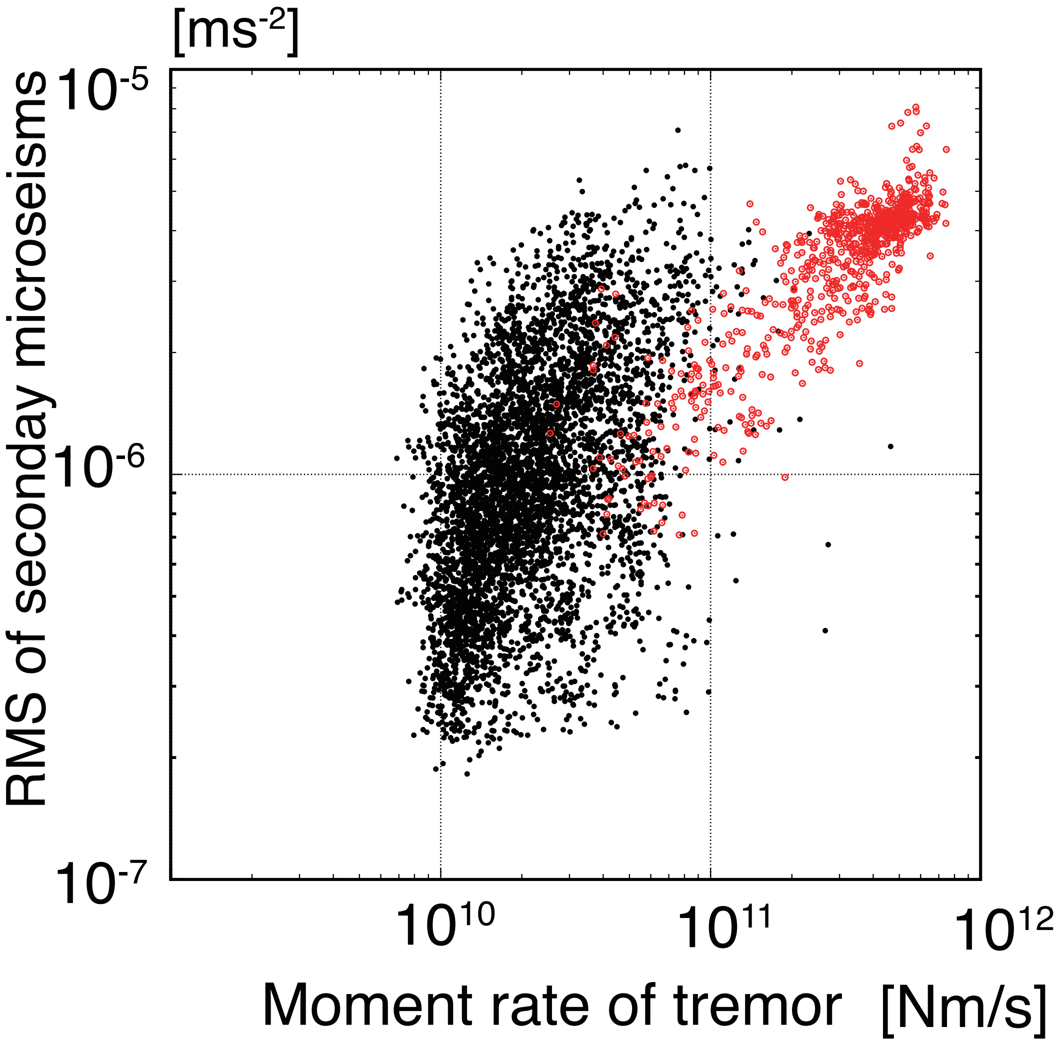

Figure 11. Scatter plot showing RMSs of the moment release rate against those of secondary microseisms. Black dots show quiet periods of the tremor activity (VR < 0.5) and red dots show the detected tremors. The detected tremors occurred in periods of high ocean swell activity throughout the period.

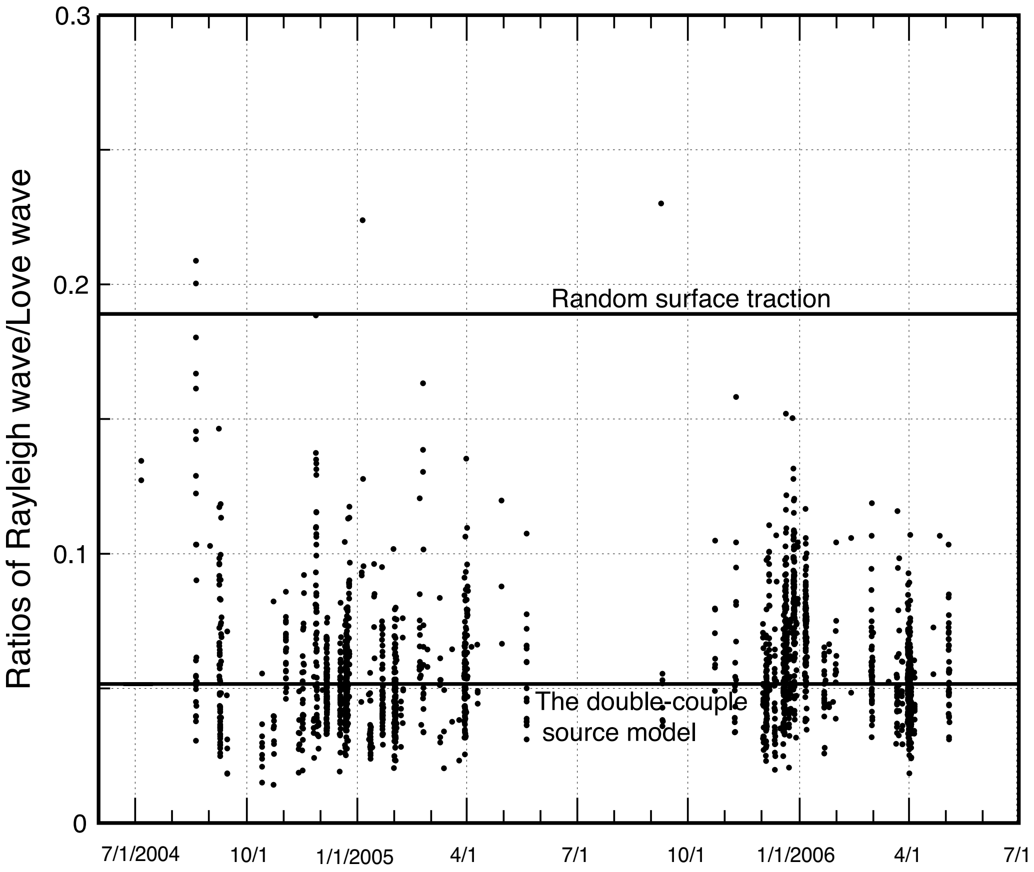

Figure 12. Plot of ratios of mean squared amplitudes of Rayleigh waves to those of Love waves. We also include theoretical predictions for shear traction on the seafloor and the double-couple source model. The ratios of primary microseisms are about 0.5 in this area [*Nishida et al.*, 2008b].

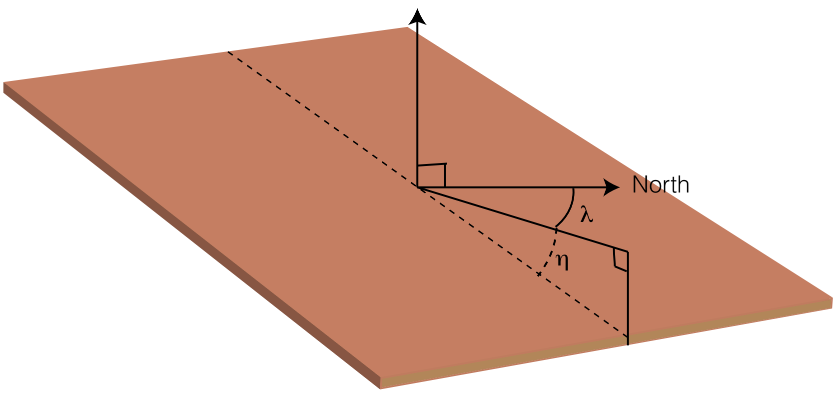

Figure 13. Definition of the dip angle η of the modeled crack and the dip direction λ. A fluid reservoir is connected to the crack.

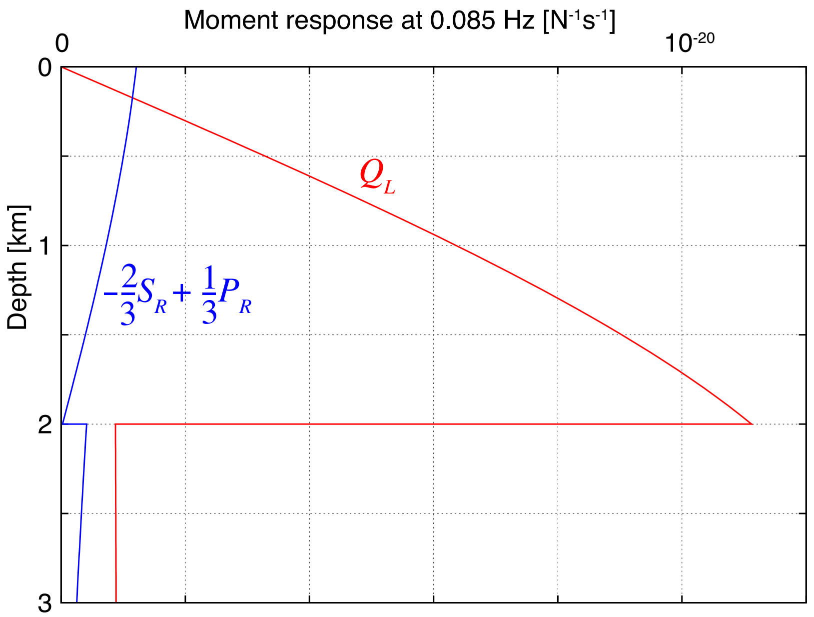

Figure 14. Moment response functions for a CLVD source and $M_{r\theta}$ (and $M_{r\phi}$).